Nano Research

Open Access

Research Article

In-situ biosynthesis of melanin by genetically engineered probiotics for efficient treatment of acute radiation enteritis

Yu Liu[1,2,§], Meng He[1,2,§], Jing Huang[1,2], Zhen Yan[1,2], Yuting Zhu[1,2], Ruoyao Cao[1,2], Fan Yu[1,2], and Jie Lu[1,2] ✉

[1] *Department of Radiology and Nuclear Medicine, Xuanwu Hospital, Capital Medical University, No. 45 Changchun St, Xicheng District, Beijing 100053, China*
[2] *Beijing Key Laboratory of Magnetic Resonance Imaging and Brain Informatics, Beijing 100053, China*
[§] *Yu Liu and Meng He contributed equally to this work.*

Cite this article: *Nano Research*, **2026**, *19*, 94908605. https://doi.org/10.26599/NR.2026.94908605

ABSTRACT: Acute radiation enteritis (ARE) commonly limits escalation during abdominopelvic radiotherapy, and conventional therapies are ineffective in reversing tissue damage. This study introduces EcN_{Tyr}, a genetically engineered probiotic created through a synthetic biology-nanomedicine approach. Based on the clinical-grade probiotic *Escherichia coli* Nissle 1917 (EcN), this strain integrates three core functional modules through comprehensive engineering. By knocking out the genes of chorismate competitive pathways (Δ*pheA*/Δ*trpR*/Δ*pykA*) and optimizing codon expression for tyrosinase, melanin could be effectively biosynthesized *in situ* in the intestinal tract. Targeted colonization facilitated by F1 fimbriae, along with the covalent binding of melanin quinones to mucin, increased EcN_{Tyr} adhesion to the inflamed lesions by fourfold over wild-type EcN and achieved prolonged local retention. In murine ARE models, EcN_{Tyr} demonstrated a therapeutic effect by mitigating oxidative stress and inflammation (by modulating IL-6, tumor necrosis factor-*α* (TNF-*α*)), restoring gut microbiota composition (by enriching *Bacteroidetes/Akkermansiaceae*, reducing pathogenic *Proteobacteria*), and regulating genes associated with intestinal repair. Transcriptome analysis further demonstrated that EcN_{Tyr} treatment reprogrammed intestinal gene expression profiles, attenuating inflammation-associated signaling while restoring metabolic and redox homeostasis programs. This "colonization-synthesis-repair" system addresses conventional probiotic limitations, offering a safe, efficient, and translatable precision therapy for radiation-induced tissue injury.

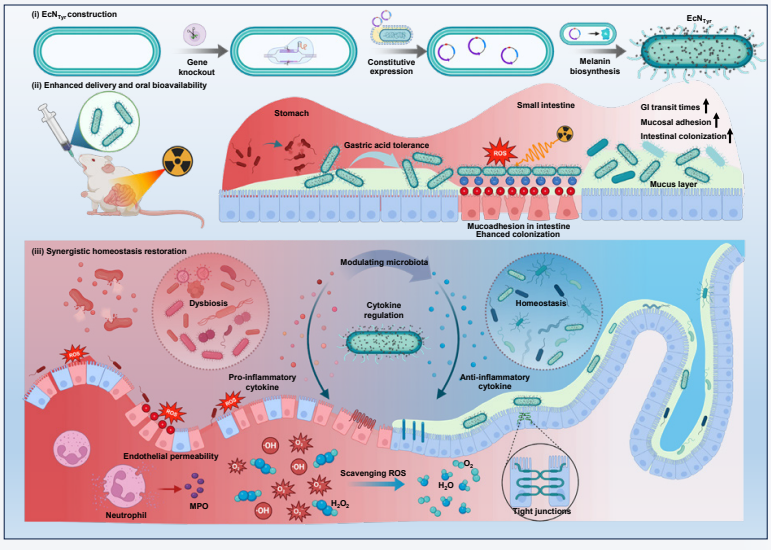

KEYWORDS: synthetic biology, melanin, gut microbiota, acute radiation enteritis

1 Introduction

Acute radiation enteritis (ARE) constitutes a dose-limiting toxic response associated with abdominal and pelvic radiotherapy. The incidence of ARE remains notably high, affecting up to 75% of patients with limited effective prevention and treatment options. Approximately 50% of individuals receiving abdominopelvic radiotherapy experience chronic intestinal issues, such as abdominal pain, diarrhea, hematochezia, and intestinal obstruction, which significantly impact their quality of life [1, 2]. The pathogenesis of ARE is multifactorial and encompasses several key mechanisms: (i) Direct DNA damage to intestinal epithelial cells by ionizing radiation, which is associated with inflammatory responses mediated by multiple signaling pathways; (ii) mitochondrial damage triggering the overproduction of reactive oxygen species

Received: December 2, 2025; **Revised:** February 24, 2026
Accepted: February 27, 2026

✉Address correspondence to imaginglu@hotmail.com

(ROS), which exacerbates lipid peroxidation and genomic instability via the Fenton reaction; and (iii) disruption of vascular endothelial cell junction proteins, causing microcirculatory leakage and creating a local ischemia-reperfusion environment that impedes tissue repair [3]. Radiation disrupts the intestinal microecological balance by reducing beneficial microbiota such as *Bifidobacterium* and *Akkermansia*, while concurrently increasing conditional pathogens such as *Enterococcus* and *Clostridium* [4–6]. This dysbiosis exacerbates inflammation in the host intestinal microenvironment, perpetuating a detrimental cycle of radiation-dysbiosis-inflammatory storm [7].

Current clinical interventions have significant limitations. First, aminosalicylates target only cyclooxygenase-2 (COX-2) to alleviate symptoms without promoting tissue repair [8]. Second, mucosal protectants like sucralfate are susceptible to dissociation and reduced efficacy in radiation environments due to their instability. Third, broad-spectrum antibiotics, while effective against conditional pathogens, further disrupt the microbial balance [9]. Although fecal microbiota transplantation can partially restore microbial diversity [10], its clinical application is hindered by challenges such as donor variability, infection risks, and uncertain efficacy [11].

Synthetic biology provides innovative approaches for precisely regulating the gut microenvironment, with engineered probiotics demonstrating potential for the targeted delivery of therapeutic molecules [12, 13]. However, traditional systems encounter several fundamental challenges: (i) Non-probiotic vectors, such as *E. coli* MG1655, raise biosafety concerns [14, 15]; (ii) inadequate gastric acid tolerance leads to low colonization efficiency and reduced efficacy [16–19]; (iii) many engineered bacteria reported in the literature demonstrate single-functionality, such as solely secreting IL-10 or transforming growth factor-β (TGF-β), which fails to address the multidimensional pathological features of ARE [12, 20–24]. Current delivery systems, like calcium alginate microspheres, improve gastric acid tolerance. However, they encounter challenges related to instability and complex preparation processes. Moreover, the toxicity of carriers like chitosan can cause goblet cell apoptosis, thereby limiting their clinical application [25–27].

Our previous research has identified melanin, a natural antioxidant, as capable of scavenging ROS through a quinone-semiquinone redox cycle. The phenolic hydroxyl groups on its surface form multiple hydrogen bonds with mucin glycan chains, facilitating targeted enrichment at inflamed sites and mitigating systemic side effects [28, 29]. Nevertheless, exogenous melanin is constrained by pharmacokinetic limitations, including low bioavailability and rapid metabolic clearance [30]. Current melanin biosynthesis systems mainly use non-probiotic hosts like *Escherichia coli* (*E. coli*), Bacillus, and Pichia pastoris, with tyrosinase activity restricted by the availability of intracellular tyrosine [31, 32]. To meet the challenge of ARE treatment, longer-lasting local effects and better combined interventions for multiple injury mechanisms are urgently needed.

This study presents a genetically engineered probiotic (EcN_{Tyr}) developed using a "synthetic biology-nanomedicine" approach, originating from the clinical-grade probiotic *E. coli* Nissle 1917 (EcN). The genes of chorismate competitive pathways (Δ*pheA*/Δ*trpR*/Δ*pykA*) were knocked out to alleviate the metabolic bottleneck associated with aromatic amino acid synthesis. Meanwhile, a tyrosinase gene sourced from *Verrucomicrobium spinosum* was optimized through codon mutation, to facilitate the high-efficient biosynthesis of melanin (nanoMel) *in situ*. The inflammation-targeted colonization facilitated by F1 fimbriae, along with the covalent binding of the quinone structure of melanin to mucin, allow EcN_{Tyr} to specifically adhere to the intestinal inflammatory lesions. This establishes a positive feedback loop of "colonization-synthesis-anchoring", which significantly extends the duration of local action. The multifaceted protective system against ARE may involve several mechanisms, including chemical scavenging, biological regulation, and structural repair (Scheme 1). NanoMel-driven antioxidant activity establishes an antioxidant barrier within the radiation microenvironment. Short-chain fatty acids and other active metabolites produced by EcN competitively inhibit pathogenic bacterial proliferation, thereby reshaping the homeostasis of intestinal microbiota. The physical barrier formed by melanin adhesion further synergizes to promote the repair of intestinal epithelial barrier integrity. The therapeutic performance of EcN_{Tyr} was explored in an ARE mouse model abdominally exposed to X-rays, and the related mechanisms of radiation protection were elucidated.

2 Results and discussion

2.1 Construction and characterization of the genetically engineered EcN_{Tyr}

Using *E. coli* Nissle 1917 (EcN) as the chassis strain, we genetically engineered it to express the tyrosinase gene, thereby generating EcN_{Tyr}, a genetically engineered probiotic that produces melanin. This study compared the catalytic efficiency of tyrosinase from *Bacillus megaterium* (*B. megaterium*) and VsTYR (M235A/N229H) from *Verrucomicrobium spinosum* (*V. spinosum*) in melanin biosynthesis (Fig. S1 in the Electronic Supplementary Material (ESM)). Under identical culture conditions, the medium of the *Bacillus megaterium* tyrosinase strain appeared lighter in color compared with that of the *V. spinosum* VsTYR (M235A/N229H) strain. Quantitative analysis showed that the melanin yield of the *B. megaterium* tyrosinase strain was approximately 0.33 mg/mL, whereas the *V. spinosum* tyrosinase strain produced approximately 0.52 mg/mL (Fig. S2 in the ESM), indicating that the *V. spinosum* enzyme has higher catalytic efficiency. Consequently, the *V. spinosum*-derived tyrosinase strain was selected for subsequent experiments. We additionally incorporated the *V. spinosum* VsTYR (M235A/N229H) gene into a previously engineered chassis strain of probiotic 1917 bacteria [33]. This strain had been modified through the knockout of the *pheA*, *trpR*, and *pykA* genes, which are involved in the competing pathways of tyrosine biosynthesis. Polymerase chain reaction (PCR) results suggested that we successfully constructed the *E. coli* Nissle 1917 Δ*pheA*Δ*trpR*Δ*pykA* engineered strains (Fig. S3 in the ESM).

As incubation time increased, the original strain EcN showed increased turbidity in the culture medium but consistently retained a golden yellow color. After the addition of copper ions and L-tyrosine to the medium, the hue of the EcN_{Tyr} bacterial culture transitioned from golden yellow to light brown and ultimately to dark brownish black as incubation time increased, attributable to the sustained synthesis of melanin (Fig. 1(a)). L-Tyrosine was initially converted to dopa through tyrosinase catalysis, followed by oxidation to dopaquinone mediated by the same enzyme. The resulting dopaquinone underwent rearrangement to form either 5,6-

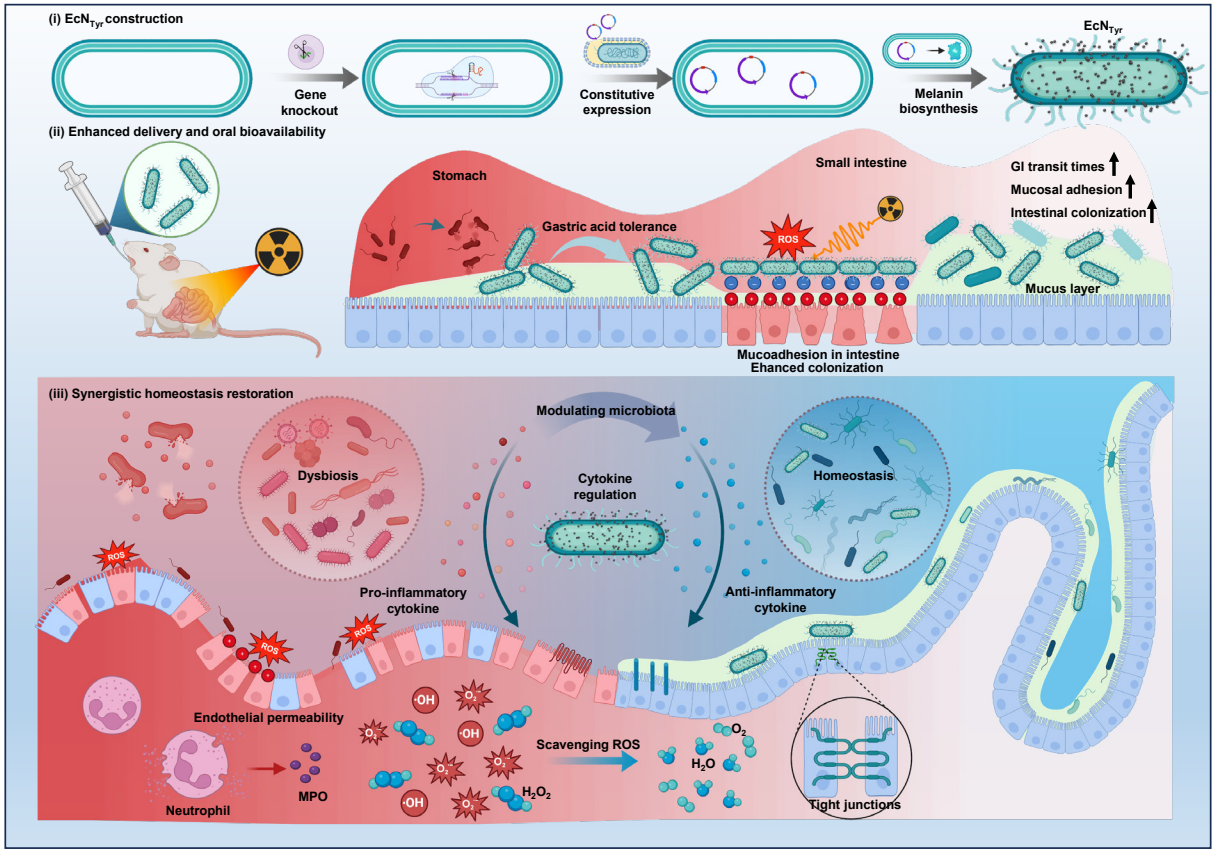

Scheme 1 A graphical representation of the therapeutic approaches of oral EcN$_{Tyr}$ for the treatment of ARE.

dihydroxyindole or 5,6-dihydroxyindole-2-carboxylic acid, which subsequently polymerized spontaneously to yield melanin. The addition of copper ions significantly enhanced the melanin synthesis rate. Ultraviolet (UV)–visible absorption spectroscopy revealed that the absorbance of both EcN and EcN$_{Tyr}$ bacterial cultures increased progressively with incubation time. At the same timepoint, the optical absorption values of EcN$_{Tyr}$ bacterial cultures exceeded those of EcN bacterial cultures due to melanin production (Figs. 1(b) and 1(c)).

The absorbance measurements of EcN and EcN$_{Tyr}$ at 600 nm at different time points indicated that expression of the *Tyr* gene did not affect the growth of the engineered probiotics (Fig. 1(d)). The UV–visible absorption spectra showed that, following the subtraction of the solution background, the primary distinction between EcN and EcN$_{Tyr}$ is the synthesis of melanin. The increased absorption beyond 300 nm is attributed to melanin, exhibiting a pronounced absorption peak of 300–400 nm, which was a typical feature of its conjugated structure, and decreased steadily with increasing wavelength. Furthermore, we analyzed the absorption spectra of all reagents incorporated during the engineered probiotic culture process. The reagents such as $CuSO_4$ exhibited weak light absorption between 300–850 nm and exert negligible influence on the bacterial solution's absorption (Fig. 1(e)), aligning with findings documented in the literature [34, 35]. Moreover, the absorbance at 800 nm of extracted nanoMel was linearly dependent on its mass concentration ($R^2 = 0.9996$) (Fig. S4 in the ESM).

The centrifugal supernatants of bacterial cultures precipitated with high concentration of hydrochloric acid were used and purified by centrifugation to yield nanoMel, the melanin nanoparticles secreted by the bacteria. The nanoMel was lyophilized, weighed for quantification, and calculated to contain approximately 0.52 mg of nanoMel per 1 mL of bacterial supernatant. We observed the morphology of the EcN and EcN$_{Tyr}$ bacterial cultures using the electron microscopy (Fig. 1(f)). Scanning electron microscopy revealed that the morphology of both EcN and EcN$_{Tyr}$ bacteria exhibited rod-shaped, with the length of EcN$_{Tyr}$ bacteria surpassing that of EcN, potentially attributable to the incorporation of external genes and the microenvironment of the culture medium. Transmission electron microscopy (TEM) demonstrated distinct differences between the strains. EcN$_{Tyr}$ displayed an irregular, thick dark black ring at its periphery, attributable to melanin deposition, while EcN lacked this feature. TEM of centrifuged supernatants from EcN cultures exhibited a clear background devoid of nanostructures, whereas EcN$_{Tyr}$ cultures contained spherical melanin nanoparticles (Fig. 1(g)). The quantitative analysis demonstrated that the size of EcN was about 1100 nm, whereas the size of EcN$_{Tyr}$ was roughly 1750 nm, possibly attributable to the insertion of exogenous genes and changes in culture conditions. The extracted melanin nanoparticles measured around 50 nm in diameter (Fig. 1(h)). In addition, literature indicated that the characteristic fourier transform infrared spectroscopy (FTIR) peaks of melanin typically appeared at 3300–3500 cm^{-1} (O–H/N–H); 1620–1650 cm^{-1} (aromatic C=C); 1500–1550 cm^{-1} (indole skeleton); and 1200–1300 cm^{-1} (C–O). These characteristics collectively confirm the presence of polyaromatic structures, phenolic hydroxyl groups, and oxidative polymerization, which are commonly found in melanin from various sources. In our study, the FTIR spectra of engineered probiotics, extracted nanoMel and commercial melanin standards all showed prominent peaks in these ranges (Fig. 1(i)). These results

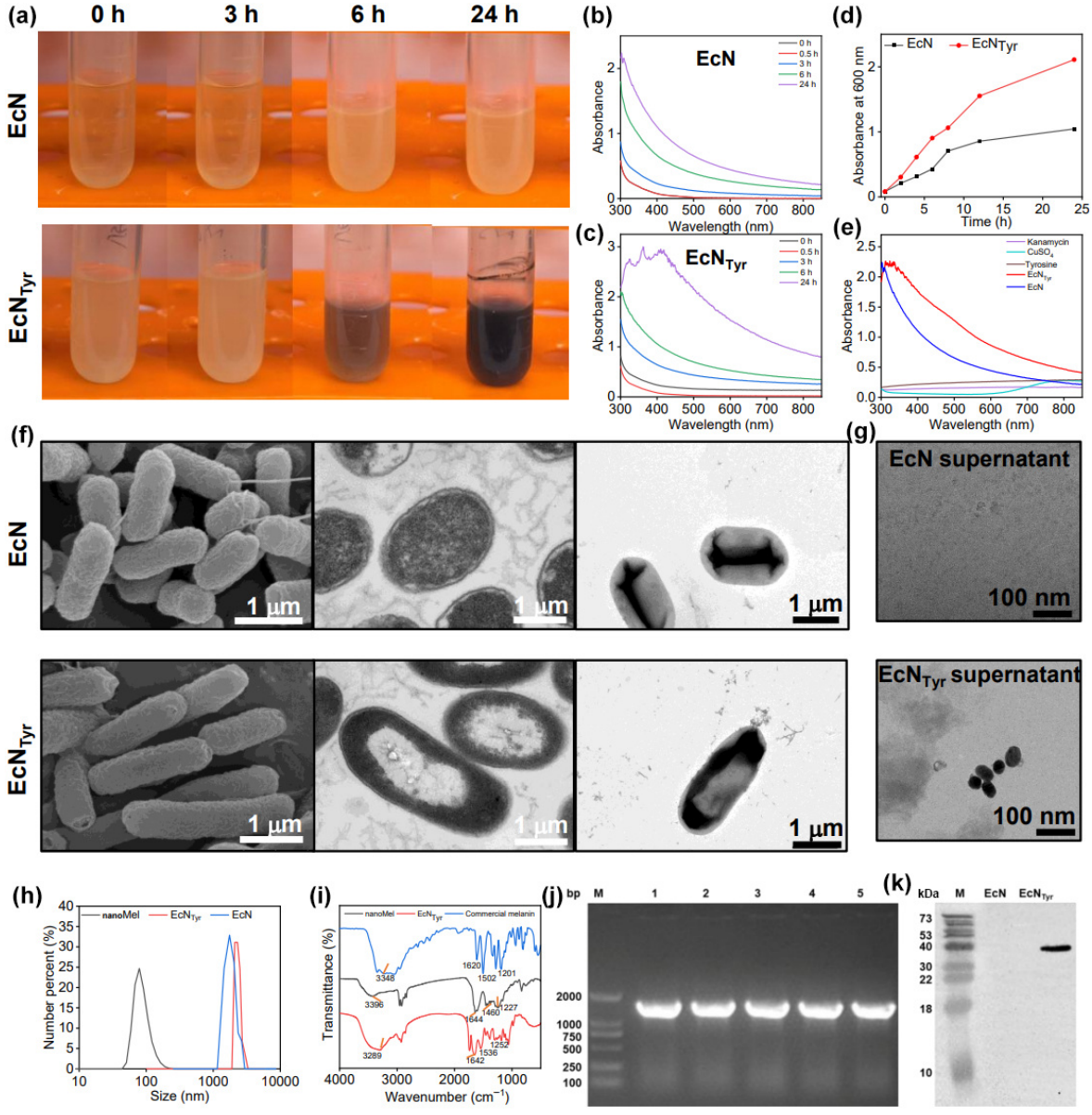

Figure 1 Construction and characterization of the genetically engineered probiotics EcN_{Tyr}. (a) General images of EcN and EcN_{Tyr} bacterial cultures at different time points. UV–visible absorption spectra of (b) EcN and (c) EcN_{Tyr} cultures at different time points detected by full-wavelength microplate readers. (d) The absorbance values of EcN and EcN_{Tyr} at 600 nm at different time points. (e) The UV–Vis absorption of EcN, EcN_{Tyr} and substrates added in EcN_{Tyr} culture for 24 h. (f) Scanning electron microscopy, biological transmission electron micrographs, transmission electron microscopy of bacterial cultures, and (g) transmission electron micrographs of centrifuged supernatants from cultures of EcN and EcN_{Tyr}, presented from up and down. (h) Size of nanoMel extracted from centrifuged supernatants of EcN and EcN_{Tyr} bacterial cultures. (i) Fourier-transform infrared spectrometer detected chemical functional groups of EcN_{Tyr}, commercial melanin and nanoMel. (j) PCR identification of EcN_{Tyr} colonies (n = 5). (k) WB expression levels of EcN and EcN_{Tyr}.

collectively demonstrated the successful biosynthesis of melanin by the genetically engineered probiotics EcN_{Tyr} and the melanin structural consistency of our product with known references [36].

The PCR results of the engineered probiotics EcN_{Tyr} and the Western blot (WB) results of EcN_{Tyr} and EcN validated the expression of the *Tyr* gene. The WB results verified that ECN_{Tyr} expressed tyrosinase (Tyr protein), with a distinct band at 38.7 kDa. Conversely, the non-engineered EcN did not exhibit the expression of the *Tyr* gene. These results indicated the successful development of the engineered probiotics EcN_{Tyr} (Figs. 1(j) and 1(k)).

2.2 Gastrointestinal stability and intestinal colonization

Oral administration is favored for gastrointestinal treatments due to its ease and high patient compliance, while also reducing side effects linked to intravenous methods. However, the gastrointestinal tract's harsh conditions challenge oral therapeutics, as oxidative stress from ROS can damage biomolecules and the intestinal lining [37]. The stability of orally administered EcN_{Tyr} in gastrointestinal fluids was tested, and their free radical scavenging abilities, comprising superoxide anions ($\cdot O_2^-$), hydroxyl radicals (·OH), 2,2-diphenyl-1-picrylhydrazyl (DPPH·) and hydrogen peroxide (H_2O_2) and nitric oxide (·NO), were analyzed by electron spin resonance spectroscopy (ESR). The ESR spectrum indicates that EcN_{Tyr} exhibits a broad capacity for scavenging H_2O_2, ·NO, $\cdot O_2^-$, ·OH and DPPH· free radicals, evidenced by the weakening of the electron spin resonance signal of the characteristic peak compared to the

control (Figs. 2(a)–2(d), and Fig. S5 in the ESM). The results showed that SDF-EcN$_{Tyr}$, when incubated with EcN$_{Tyr}$ and gastrointestinal simulation fluid, had a similar ESR signal attenuation to EcN$_{Tyr}$, indicating that the fluid did not significantly impact EcN$_{Tyr}$'s free radical scavenging ability. In contrast, EcN had minimal capacity to scavenge H_2O_2, $\cdot O_2^-$, ·NO, ·OH and DPPH· free radicals. These results showed that EcN$_{Tyr}$ possessed promise for antioxidant therapy and favorable gastrointestinal stability and was anticipated to be utilized for oral delivery to treat diseases related to gastrointestinal oxidative stress damage. Consistent with the ESR results, colony formation and CFU assays further demonstrated that EcN$_{Tyr}$ maintained favorable viability after SDF treatment. The Vs-EcN$_{Tyr}$ showed significantly higher survival after 2 h of SDF treatment than EcN and Bm-EcN$_{Tyr}$, supporting its suitability for oral delivery (Figs. 2(e)–2(g)).

For therapeutic efficacy, orally delivered formulations must effectively retain and accumulate in the inflamed intestine. To evaluate the intestinal colonization and retention capacity of engineered probiotics, EcN and EcN$_{Tyr}$ were labeled with IR-dye800 and tracked using *in vivo* imaging system (IVIS) in an ARE mouse model. Following oral administration, longitudinal fluorescent imaging revealed distinct colonization dynamics between the two groups (Fig. 2(h)). The EcN group exhibited transient abdominal fluorescence signals that peaked at 2 h and declined rapidly, with substantially diminished signals observed at 8 and 24 h. In contrast, EcN$_{Tyr}$ demonstrated markedly prolonged signal retention within

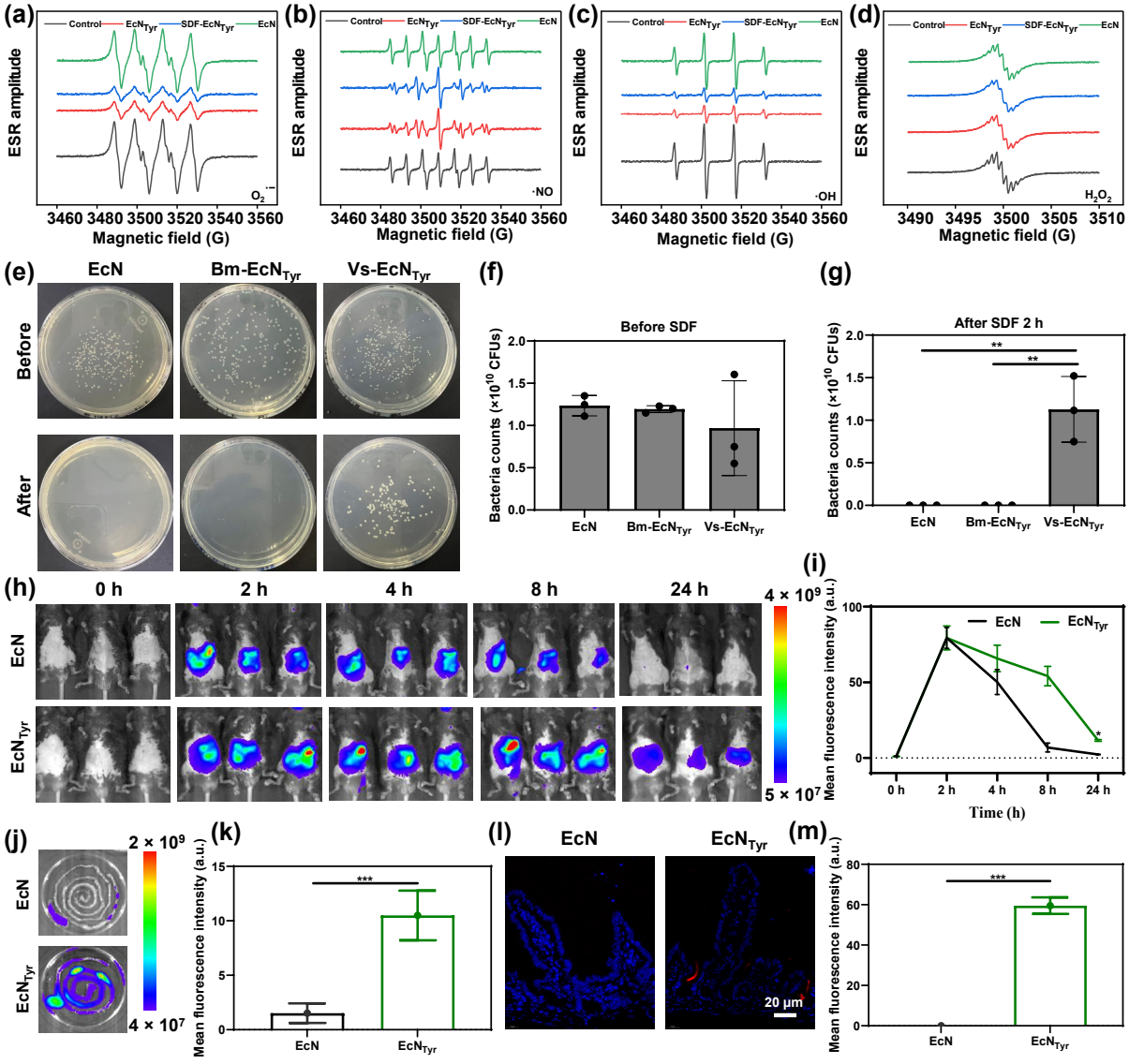

Figure 2 Gastrointestinal stability and intestinal colonization ability of genetically engineered probiotics EcN$_{Tyr}$ and EcN. Evaluation of the free-radical-scavenging capacity and gastrointestinal stability of EcN$_{Tyr}$ and EcN. SDF-EcN$_{Tyr}$ denotes EcN$_{Tyr}$ sequentially treated with gastric and intestinal fluid simulants to mimic gastrointestinal transit after oral gavage. The ESR spectrometer was used to detect the scavenging ability of EcN, EcN$_{Tyr}$, and SDF-EcN$_{Tyr}$ for (a) H_2O_2, (b) ·NO, (c) O_2^-, and (d) ·OH radicals before and after treatment with gastrointestinal simulant. (e) Colony formation assays of EcN, Bm-EcN$_{Tyr}$, and Vs-EcN$_{Tyr}$ before and after SDF treatment. (f) CFU per milliliter (×10^{10}) of each group before SDF treatment. (g) CFU per milliliter (×10^{10}) of each group after SDF treatment. (h) *In vivo* IVIS imaging of IR-dye800-labeled EcN and EcN$_{Tyr}$ following oral administration in a radiation-injured mouse model at 0, 2, 4, 8, and 24 h. (i) Quantification of mean fluorescence intensity of EcN and EcN$_{Tyr}$ at different time points. (j) *Ex vivo* fluorescence imaging of excised intestinal tissues from radiation-injured mice. (k) Quantification of mean fluorescence intensity of excised intestinal tissues. (l) Fluorescence imaging of intestinal tissue sections. (m) Quantification of mean fluorescence intensity of intestinal tissue sections. Data was from the mean ± standard deviation of at least three independent experiments. Statistical differences: $^*P < 0.05$, $^{**}P < 0.01$, $^{***}P < 0.001$.

the abdominal region, with strong fluorescence persisting up to 24 h post-administration. Quantitative analysis confirmed significantly higher mean fluorescence intensity in the EcN_{Tyr} group compared with the EcN group across multiple time points (Fig. 2(i)). Consistent with the *in vivo* observations, *ex vivo* fluorescent imaging of excised intestinal tissues further demonstrated enhanced accumulation of EcN_{Tyr} in the inflamed intestine (Fig. 2(j)). Quantification of fluorescence intensity showed that the EcN_{Tyr} group exhibited a 6.89-fold increase in intestinal signal compared with the EcN group (Fig. 2(k)). Moreover, fluorescence imaging of intestinal tissue sections provided histological-level evidence of localized probiotics retention, revealing a 59.526-fold higher fluorescence signal in the EcN_{Tyr} group relative to EcN controls (Figs. 2(l) and 2(m)). Fontana-Masson staining revealed clear melanin deposits in the intestinal tissues of mice treated orally with EcN_{Tyr}, whereas the EcN control group showed no melanin staining (Fig. S6 in the ESM). The findings indicated that EcN alone may exhibit inadequate retention capability in intricate gastrointestinal environment, while EcN_{Tyr} specifically targeted inflammatory intestinal regions, hence extending accumulation and retention durations.

Enhanced colonization and prolonged retention of EcN_{Tyr}-based constructs in inflamed intestinal segments have been reported previously [38]. Consistent with these studies, the observed phenomenon may be attributed to the following plausible mechanisms: (1) The disrupted mucosal layer in inflamed intestinal segments expresses abundant positively charged proteins, creating a net positive charge on the mucosal surface that provides natural targeting sites for negatively charged bacteria and melanin (Mel). (2) The compromised intestinal barrier with increased permeability in diseased segments, combined with Mel's strong mucoadhesive properties, synergistically prolongs retention time. (3) As a dominant commensal bacterium, *E. coli* exhibits inherent homing capability to inflamed intestinal regions. These features may collectively help explain the enhanced targeted colonization and prolonged retention of EcN_{Tyr} in inflamed intestinal segments.

2.3 The therapeutic benefits of EcN_{Tyr} for ARE observed *in vivo*

The clinical application of nanomedicine necessitates the consideration of biocompatibility. We assessed biocompatibility both *in vitro* and in animal models. Peripheral blood hematology after different treatments suggested minimal toxicity (Fig. S7(a) in the ESM). At different time points (days 0, 3, 7, and 14) after oral delivery of EcN_{Tyr} to healthy mice, no significant differences were observed in the diverse hematological parameters (Fig. S7(b) in the ESM), suggesting that the oral delivery of EcN_{Tyr} did not significantly impact these peripheral blood hematological indicators. The results of serum biochemical index detection showed (Fig. S7(c) in the ESM) that the parameters of various indicators at different time points fluctuated, but most of them were within the normal reference range. Reliable biosafety is essential for the *in vivo* application of novel agents and future clinical transformation. We evaluated the biosafety of EcN_{Tyr} at both cellular and animal levels. The outcomes of the cell proliferation and toxicity assay revealed that across the tested concentration range, nanoMel treatment did not significantly impact the viability of Hiec cells (Fig. S7(d) in the ESM). At the concentration of 200 μg/mL, the cell viability rate exceeded 85%, demonstrating that nanoMel exhibits favorable biocompatibility at the cellular level. The results of hematoxylin and eosin (H&E) staining showed that no obvious histological abnormalities or structural damage were observed in the light microscopic structures of various tissues and organs at different time points (Figs. S8 and S9 in the ESM). The above results collectively indicated that EcN_{Tyr} possessed favorable biosafety and is appropriate for subsequent biological applications.

Considering the favorable biocompatibility, gastrointestinal stability, and extensive free-radical scavenging efficacy of EcN_{Tyr}, we conducted a thorough assessment of the therapeutic efficacy of oral administration of EcN_{Tyr} in the ARE mouse model (Fig. 3(a)). The histological inflammation score of the small intestine provided direct evidence for assessing the treatment effect. Hematoxylin and eosin staining (Fig. 3(b)) suggested that, in contrast to the healthy control group, the small intestinal tissue of the ARE mouse model group exhibited significant morphological and structural abnormalities. These abnormalities included atrophy and loss of intestinal crypts, thickening of the basement membrane, epithelial erosion and desquamation with denudation of the lamina propria, disappearance of normal goblet cells accompanied by severe mucosal gland defects, mucosal ulcers, and widespread infiltration of inflammatory cells. These features indicated the successful establishment of the ARE mouse model. Following EcN_{Tyr} treatment, the arrangement of small intestinal mucosal epithelial cells and mucosal glands appeared organized and compact, exhibiting no significant reduction or desquamation, decreased inflammatory cell infiltration, significantly lower histopathological scores (Fig. 3(c)), and the depth of small intestinal crypts reverted to normal levels, while the EcN treatment group was not significantly relieved (Figs. 3(d) and 3(e)).

Comparative histological analysis revealed significant structural alterations in the small intestinal villi of model group mice relative to healthy controls, characterized by extensive collapse, architectural disruption, and tissue loss. EcN_{Tyr} treatment markedly improved villus integrity reduced mucosal damage, and restored goblet cell populations (Figs. 3(f) and 3(g)). Immunohistochemical (IHC) assessment of Ki67 and terminal deoxynucleotidyl transferase dUTP nick end labeling (TUNEL) staining demonstrated decreased proliferative activity and increased apoptotic cell numbers in model group intestinal tissues, but EcN treatment group had no significant recovery (Figs. 3(h)–3(k)). EcN_{Tyr} administration effectively enhanced cellular proliferation while reducing apoptosis in intestinal tissues. These findings collectively indicate that EcN_{Tyr} treatment can ameliorate histopathological abnormalities in the ARE mouse model.

2.4 Evaluation of antioxidative stress and anti-inflammatory performance of EcN_{Tyr}

Considering that EcN_{Tyr} possessed extensive free radical scavenging capabilities, we employed the 2',7'-dichlorodihydrofluorescein diacetate (DCFH-DA) fluorescent probe to evaluate the effect of nanoMel on intracellular ROS levels. Following lipopolysaccharide (LPS) stimulation, bright green fluorescence was detected in RAW 264.7 cells, signifying elevated intracellular ROS levels. Following nanoMel treatment, the fluorescence intensity of the cells markedly diminished, demonstrating that nanoMel could effectively scavenge intracellular ROS (Fig. 4(a) and Fig. S9 in the ESM). Similarly, following H_2O_2 treatment, bright green fluorescence was observed in Hiec cells, signifying elevated intracellular ROS levels. Following nanoMel treatment, the fluorescence intensity of the cells markedly diminished, indicating that nanoMel can effectively scavenge

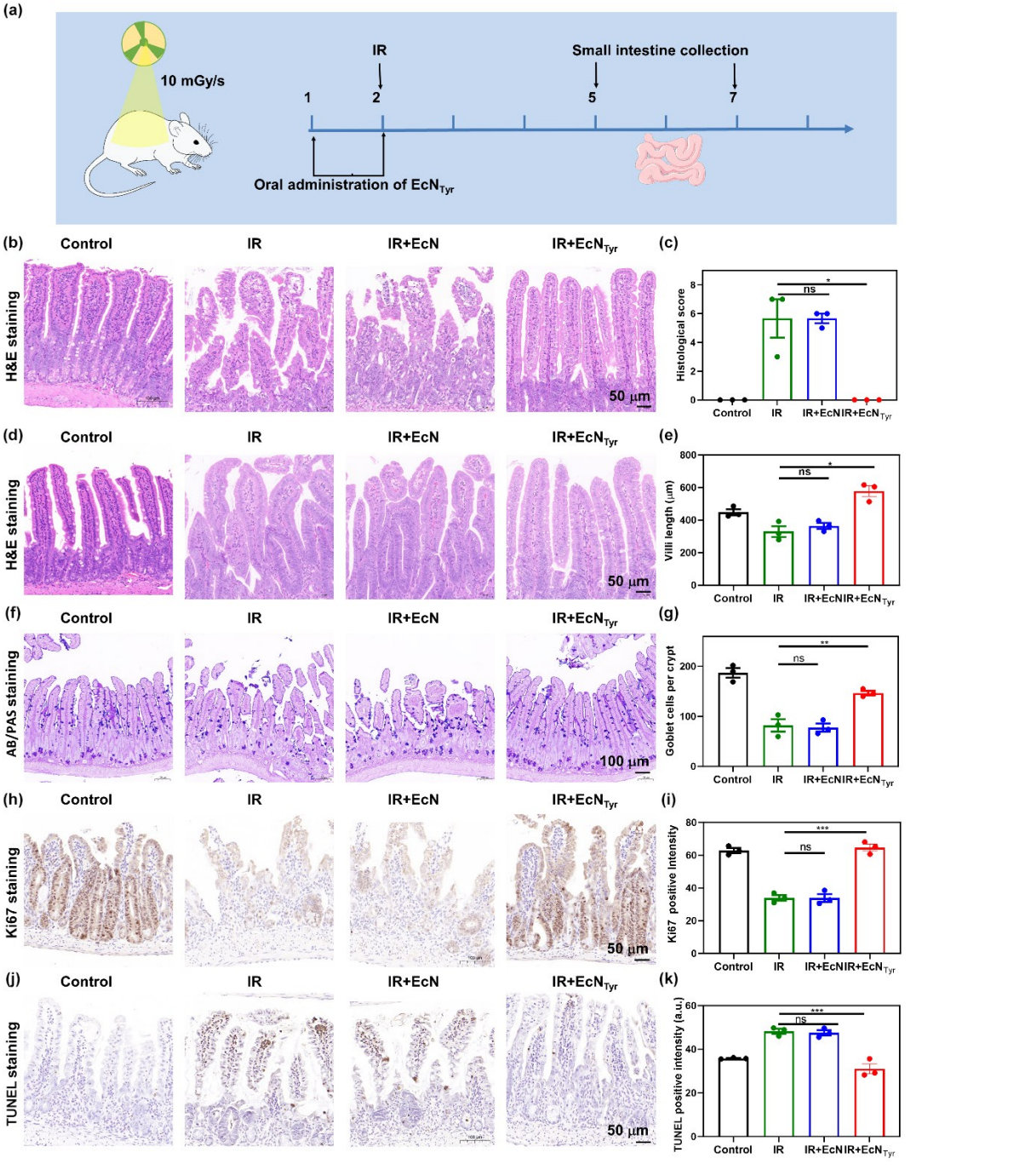

Figure 3 Evaluation of the effect of EcN and genetically engineered probiotics EcN$_{Tyr}$ in the treatment of ARE mouse model. (a) Schematic diagram of model establishment and treatment protocol. (b) H&E staining images of small intestinal tissues of mice 3 days post treatment from different groups. Scale bar: 50 μm. (c) Pathological scoring of H&E images of small intestinal tissues. (d) H&E images of small intestinal tissues of mice 3 days post treatment from different groups. Scale bar: 50 μm. (e) Crypt depth analysis of small intestinal tissues. (f) Alcian blue staining images of small intestinal tissues of mice 3 days post treatment from different groups. Scale bar: 100 μm. (g) Quantitative analysis of the number of goblet cells per crypt in small intestinal tissues. (h) IHC staining of Ki67 in small intestinal tissues of mice 3 days post treatment from different groups. Scale bar: 50 μm. (i) Semi-quantitative analysis of Ki67-positive cells. (j) IHC staining of TUNEL in small intestinal tissues 3 days of mice post treatment from different groups. Scale bar: 50 μm. (k) Semi-quantitative analysis of TUNEL-positive cells. Data was from the mean ± standard deviation of at least three independent experiments. Statistical differences: ns, not significant, $^{*}P < 0.05$, $^{**}P < 0.01$, $^{***}P < 0.001$.

intracellular ROS. Subsequently, we detected the level of ROS in the small intestinal tissue of ARE mouse model. The results showed that bright red fluorescence was detectable in the small intestinal tissue cells of the mice 3 days post treatment from different groups, indicating elevated levels of intracellular ROS (Fig. 4(b) and Fig. S11 in the ESM). The fluorescence intensity in the small intestinal tissue cells of mice treated with EcN was significantly diminished, and it was further reduced in the EcN$_{Tyr}$ group, suggesting that EcN$_{Tyr}$ can efficiently eradicate ROS in tissue cells *in vivo*.

Excessive ROS can oxidize lipids and produce abundant malondialdehyde, a biomarker indicative of oxidative stress, in the affected intestinal segment. Glutathione peroxidase is a crucial

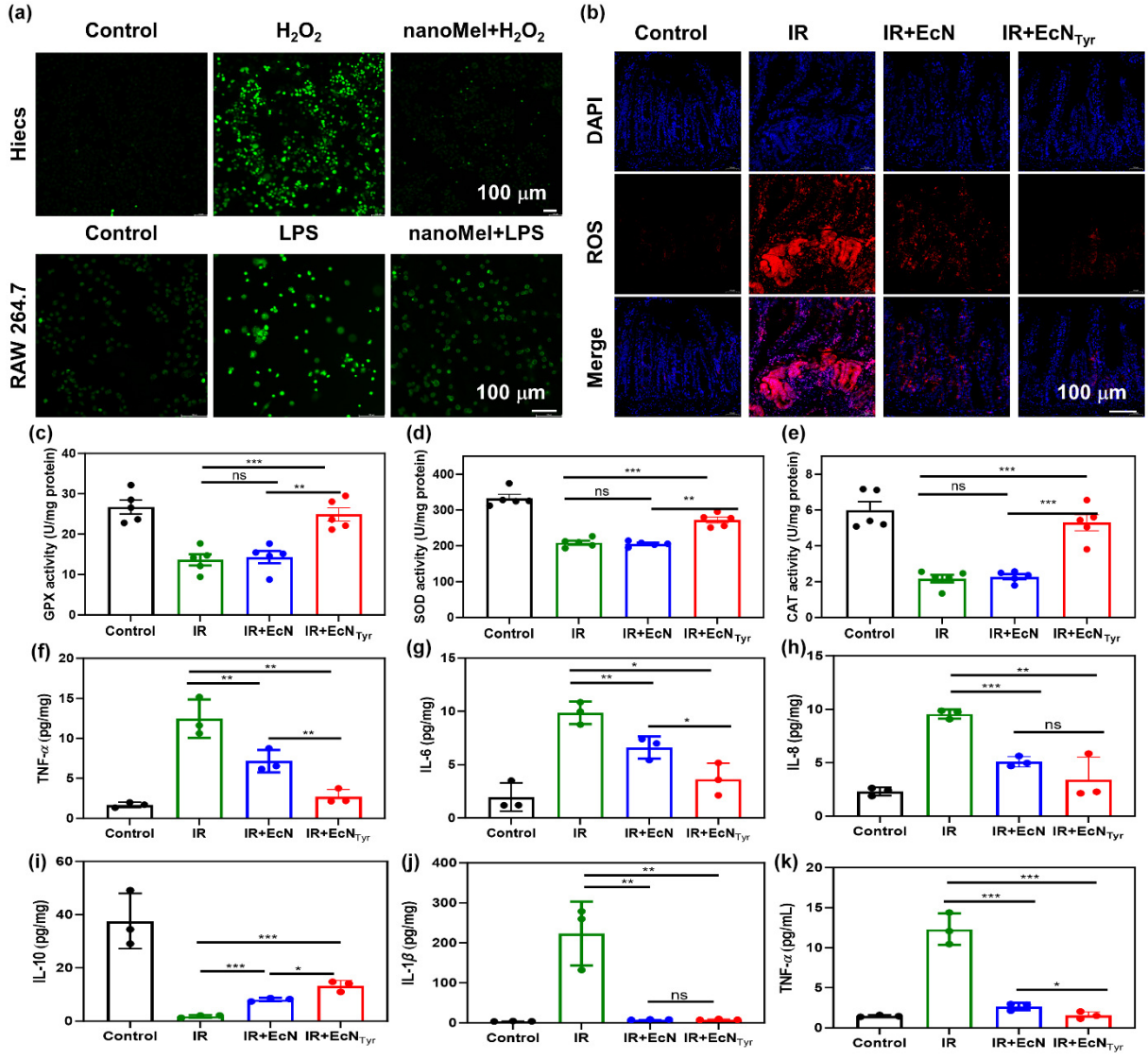

Figure 4 Evaluation of anti-oxidative stress and anti-inflammatory performance of EcN and genetically engineered probiotics EcN_{Tyr}. (a) ROS detection kit to detect the effect of nanoMel on intracellular reactive oxygen species levels. (b) ROS detection kit to detect the effect of EcN and EcN_{Tyr} on intracellular ROS levels in small intestinal tissues of ARE mouse model. The ELISA kit was used to detect (c) glutathione peroxidase activity, (d) superoxide dismutase activity, and (e) catalase activity in the small intestinal tissues of mice after 3 days of treatment. The ELISA kit to detect the levels of (f) TNF-α, (g) IL-6, (h) IL-8, (i) IL-10, and (j) IL-1β in small intestinal tissue homogenate of mice 3 days post treatment from different groups. (k) The ELISA kit to detect serum TNF-α levels 3 days post treatment from different groups. Data was from the mean ± standard deviation of at least three independent experiments. Statistical differences: ns, not significant, $^{*}P < 0.05$, $^{**}P < 0.01$, $^{***}P < 0.001$.

protein that can reduce the synthesis of malondialdehyde. We evaluated the ability of EcN_{Tyr} to reverse oxidative stress damage in small intestinal tissue by detecting the levels of malondialdehyde, and the enzymatic activities of glutathione peroxidase, superoxide dismutase, catalase, and myeloperoxidase across different groups. The findings indicated that the malondialdehyde levels in the small intestinal tissue of the mouse model were elevated, measuring 2.2 times over those of the control. Following EcN_{Tyr} therapy, the malondialdehyde levels decreased significantly (Fig. S12 in the ESM). The glutathione peroxidase activity in the small intestinal tissue of the mouse model was reduced to 51% of control levels (Fig. 4(c)), while superoxide dismutase activity decreased to 63% of normal values (Fig. 4(d)). Both antioxidant enzymes showed marked activity restoration following EcN_{Tyr} administration, whereas no relief was observed in the EcN-treated group. The catalase activity in the small intestinal tissue of the model group was reduced to 36% of healthy control levels, with a subsequent increase following EcN_{Tyr} treatment, while EcN treatment had no such effect (Fig. 4(e)). The myeloperoxidase activity showed a significant elevation in the model group intestinal tissue compared to healthy controls, indicating enhanced neutrophil recruitment. Following EcN_{Tyr} or EcN therapy, myeloperoxidase activity significantly decreased, signifying a decline in neutrophil infiltration (Fig. S13 in the ESM). The experimental data revealed elevated malondialdehyde levels accompanied by decreased activities of key antioxidant enzymes, including glutathione peroxidase, superoxide dismutase, and catalase in irradiated intestinal tissue, along with increased myeloperoxidase activity. EcN_{Tyr} can effectively reverse this phenomenon by diminishing oxidative stress in the affected intestine segment and decreasing neutrophil infiltration and activity at the lesion site.

The excessive production of ROS triggers a proinflammatory

cytokine cascade at inflammatory sites, further amplifying intracellular ROS production and establishing a vicious cycle [39]. We employed an enzyme-linked immunosorbent assay (ELISA) kit to detect the concentrations of representative inflammatory cytokines such as TNF-α, IL-6, IL-8, IL-10, and IL-1β in small intestinal tissue and serum. Comparative analysis revealed significant elevations in proinflammatory cytokines (TNF-α, IL-6, IL-8, and IL-1β) and reduction in anti-inflammatory IL-10 in model group intestinal tissues relative to healthy controls (Figs. 4(f)–4(j)). EcN treatment resulted in a modest restoration of these cytokines, while EcN_{Tyr} treatment effectively normalized these cytokine perturbations. Serum TNF-α levels followed a similar pattern, with marked increase in model animals and subsequent decrease following EcN or EcN_{Tyr} administration (Fig. 4(k)). The results demonstrate that EcN_{Tyr} can significantly decrease proinflammatory cytokine levels, elevate anti-inflammatory cytokine levels, and enhance the inflammatory microenvironment at the inflammation site.

Peripheral blood analysis across experimental groups revealed significant hematological alterations (Fig. S14 in the ESM). Compared with the healthy controls, the model group exhibited significantly increased levels of leukocytes, monocytes, lymphocytes, and neutrophils. However, these elevated levels were markedly reduced after EcN_{Tyr} treatment. Additionally, EcN treatment also demonstrated a moderate therapeutic effect. The ARE model group exhibited markedly elevated platelet counts relative to healthy controls, which were partially normalized upon EcN_{Tyr} treatment. Simultaneously, decreased red blood cell counts observed in the model group mice, attributable to bleeding from the small intestine mucosa, were effectively restored by EcN or EcN_{Tyr} intervention. These findings demonstrated EcN_{Tyr}'s capacity to modulate inflammatory and immune cell populations while restoring normal hematological parameters.

The diseased intestinal segment exhibited elevated levels of pro-inflammatory cytokines in the small intestinal mucosa, which contributed to increased intestinal permeability and exacerbated tissue damage. Restoration of barrier integrity is a critical indicator of therapeutic efficacy. Through tissue immunofluorescence staining, we quantitatively analyzed the expression of tight junction proteins ZO-1, occludin, and claudin-1 in the affected intestinal region. The results showed that compared with the healthy control, the fluorescence intensity of ZO-1, occludin and claudin-1 in the small intestinal tissue of the model group mice decreased to 7%, 16% and 29% of that observed in the healthy control group, respectively, indicating the impairment of the intestinal epithelial barrier (Fig. S15 in the ESM). EcN_{Tyr} administration resulted in marked recovery of all three tight junction proteins, with fluorescence intensity showing differential but significant improvements. EcN treatment also demonstrated moderate recovery. These findings demonstrate EcN_{Tyr}'s capacity to effectively restore intestinal epithelial barrier integrity in the affected intestinal segment. Notably, with EcN serving as the control, the superior therapeutic outcomes of EcN_{Tyr} attribute the enhanced efficacy to the *in situ* synthesized melanin.

2.5 Analysis of intestinal microbial diversity in mice after treatment

We next investigated the regulatory effect of EcN_{Tyr} on the gut microbiota in mice with radiation-induced intestinal injury and found that EcN_{Tyr} effectively alleviated intestinal dysbiosis in ARE mice, as demonstrated by multidimensional microbiota analyses. This work found that EcN_{Tyr} can effectively improve intestinal dysbiosis in mice suffering from ARE using multidimensional microbiota analysis.

2.5.1 *Alpha diversity: Injury repair*

Compared with the control group, the intestinal irradiation (IR) group presented with significantly lower microbiota abundance (Observed species, Chao1) and evenness (Shannon, Simpson) (Figs. 5(a)–5(d)), suggesting that radiation-induced injury disturbed the intestinal microenvironment and inhibited microbial colonization and proliferation. The α-diversity in the IR+ EcN_{Tyr} group approached that of the control group, indicating that EcN_{Tyr} enhanced diversity by providing beneficial bacterial substrates (such as tyrosine metabolites) and competing for colonization, demonstrating a superior effect to the EcN group. This indicates that the synthesis and expression of tyrosinase may augment substrate availability and colonization advantage to beneficial bacteria, facilitating the re-enrichment of the microbial community.

2.5.2 *β-diversity: Structural remodeling*

PCoA (Bray–Curtis distance)/non-metric multidimensional scaling (NMDS) analysis revealed distinct clustering patterns among groups, indicating marked microbial community structures among groups. The IR1 group was completely separate, while the control and IREcNTyr1 groups overlapped significantly, indicating similar microbiota compositions (Figs. 5(e) and 5(f)). The control group showed tight clustering, indicating stable gut microbiota homeostasis. In contrast, the IR group displayed dispersed distribution. Notably, the IR+EcN_{Tyr} group's profile closely resembled the control. This suggests that EcN_{Tyr} has the capacity to enhance the abundance of core functional bacteria, such as Bacteroidetes, while simultaneously inhibiting non-specific colonization. The intermediate positioning of the EcN group between IR and IR+EcN_{Tyr} groups confirmed that the synthesis and expression of tyrosinase could augment EcN's colonization efficiency and microbiota-modulating precision.

2.5.3 *Community composition: Restoration of dominant phylum function*

Phylum-level analysis revealed distinct microbial profiles (Fig. 5(g)). The control group maintained metabolic balance with *Bacteroidetes* and *Firmicutes* as dominant phyla. In the IR group, *Bacteroidetes* decreased while *Proteobacteria* (opportunistic pathogens) proliferated, leading to a dominance shift from *Bacteroidetes* to *Proteobacteria* and an aberrant activation of pro-inflammatory metabolic pathways. The IR+EcN_{Tyr} group significantly restored the proportions of *Bacteroidetes* and *Firmicutes*, promoted short-chain fatty acids (SCFA) production, and attenuated inflammation, outperforming unmodified EcN. This indicated that tyrosine modification augmented EcN's capacity to modulate core phyla.

2.5.4 *Differential taxonomic units: Target correlation for precision intervention*

LEfSe analysis identified significant enrichment of pathogenic bacteria (*Proteobacteria/Enterobacteriaceae*) in the IR group, which activated pro-inflammatory pathways (Figs. 5(h)–5(i)). In contrast, the IR+ EcN_{Tyr} group showed marked increases in beneficial bacteria (*Bacteroidetes/Bacteroidia*) that mediated anti-inflammatory effects via SCFA production and competitive exclusion of pathogens. Cladogram analysis further demonstrated

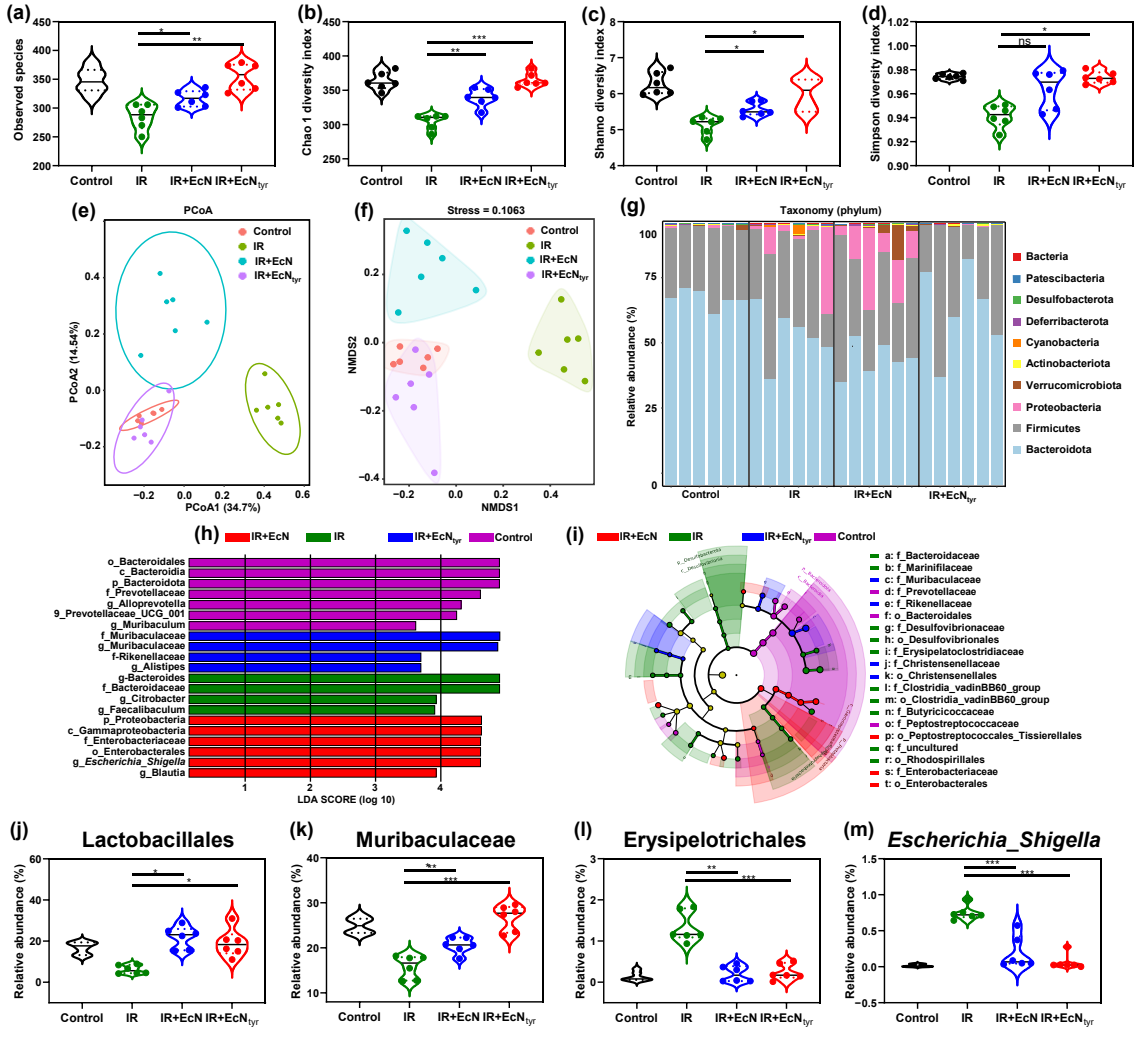

Figure 5 Analysis of intestinal microbial diversity in mice after treatment. (a) Microbial community abundance. (b) Chao 1 index (richness estimator). (c) Shannon index (diversity estimator). (d) Simpson index (diversity estimator). (e) Principal coordinate analysis (PCoA) of β-diversity in the gut microbiota. (f) NMDS of β-diversity in the gut microbiota. (g) Relative abundance of bacterial taxa at the phylum level. (h) Linear discriminant analysis (LDA) coupled with LEfSe (LDA effect size) to identify differentially abundant taxa. (i) Cladogram illustrates taxonomic differences identified by LEfSe. The relative abundance of (j) Lactobacillales, (k) Muribaculaceae, (l) Erysipelotrichales, and (m) *Escherichia_Shigella*. Statistical differences: ns, not significant, $^{*}P < 0.05$, $^{**}P < 0.01$, $^{***}P < 0.001$. $n = 6$ each group.

that EcN_{Tyr} intervention achieved superior enrichment of beneficial microbiota and more effective pathogen suppression compared to EcN alone, confirming that tyrosinase modification enhanced EcN's regulatory capacity in gut microbiota modulation.

2.5.5 *EcN_{Tyr} restores gut microbiota homeostasis after irradiation*

16S rRNA sequencing revealed gut dysbiosis in the IR group, characterized by increased *Firmicutes* abundance and a higher F/B ratio, decreased levels of Bacteroidetes, Lactobacillales, and Muribaculaceae, as well as a marked increase in Proteobacteria (particularly *Escherichia_Shigella*). Both *E. coli* Nissle 1917 EcN and EcN_{Tyr} interventions improved the microbial composition, with EcN_{Tyr} exerting a more pronounced regulatory effect. Specifically, EcN_{Tyr} significantly reduced Firmicutes, Proteobacteria, *Escherichia_Shigella*, and Erysipelotrichales, while restoring Bacteroidetes, Muribaculaceae, and Lactobacillales to levels closer to healthy controls. These changes suggest a greater potential of EcN_{Tyr} for re-establishing microbial balance, promoting beneficial bacterial colonization, restoring metabolic functions, enhancing barrier integrity, and suppressing pathogenic bacteria (Figs. 5(j)–5(m), and Fig. S16 in the ESM).

Operational taxonomic unit (OTU) Venn diagram analysis showed that the IR group had the highest number of unique OTUs, indicating severe radiation-induced dysbiosis and enrichment of abnormal taxa. The IR+EcN_{Tyr} group exhibited the fewest unique OTUs and the greatest overlap with healthy controls, suggesting that EcN_{Tyr} effectively reversed dysbiosis, reduced abnormal taxa, and promoted beneficial bacterial recovery. The healthy group displayed fewer unique OTUs, reflecting a stable core microbiota. Overall, the IR group showed reduced beneficial and increased harmful bacteria, whereas both EcN and IR+EcN_{Tyr} shifted toward the healthy profile, with EcN_{Tyr} demonstrating superior efficacy (Fig. S17 in the ESM).

2.5.6 *Core conclusion: the intervention advantages and mechanisms of EcN_{Tyr}*

EcN_{Tyr} intervention demonstrated superior therapeutic effects compared to EcN alone through tyrosinase-mediated metabolic enhancement. This synergistic approach more effectively restored microbial diversity, reestablished Bacteroidetes-dominated beneficial metabolic networks, and precisely suppressed pathogenic bacteria. The "metabolism-augmented composite remediation"

strategy, achieved through improved substrate availability, enhanced colonization capacity, and precise microbial modulation, offered a more efficient strategy for ARE therapy.

2.6 Transcriptome sequencing analysis of mouse small intestine tissues

We investigated the mechanism of EcN_{Tyr} treatment for ARE by performing transcriptome sequencing on mouse small intestine tissue. A correlation heatmap revealed analogous inner group expression patterns among the EcN_{Tyr} treatment, EcN treatment, IR, and healthy control group (Fig. S18(a) in the ESM). Principal component analysis revealed substantial variances among sample groups, while samples within the same group exhibited consistent expression levels (Fig. S18(b) in the ESM). The differential gene clustering heatmap displayed unique transcriptome profiles across the groups (Fig. 6(a)). Compared with the control group, the IR group demonstrated 1539 upregulated and 1197 downregulated genes, as illustrated in the volcano plot, emphasizing the intergroup disparities in gene expression. These results illustrate the significant disruption of gene expression profiles in small intestinal tissue resulting from acute radiation-induced intestinal injury. After EcN_{Tyr} administration, 646 genes were upregulated, and 440 genes were downregulated compared to the IR group, indicating EcN_{Tyr}'s broad potential to modulate gene expression in these tissues (Figs. 6(b) and 6(c)). The Venn diagram of differentially expressed genes identified 646 genes overlapping between the comparison of EcN_{Tyr} and IR, and the comparison of IR and control (Fig. S18(c) in the ESM).

Furthermore, Kyoto Encyclopedia of Genes and Genomes (KEGG) pathway enrichment analysis indicated that, compared with controls, the IR group exhibited prominent activation of inflammatory and stress-response pathways, including complement cascades, cytokine–cytokine receptor interaction, IL-17 signaling, and p53-mediated DNA damage response. Concurrently, pathways related to xenobiotic and drug metabolism, cytochrome P450–dependent detoxification, peroxisomal function, and retinol metabolism were suppressed, indicating impaired antioxidant capacity and metabolic homeostasis following radiation exposure (Figs. 6(d) and 6(e)). In contrast, EcN_{Tyr} treatment reshaped these transcriptional programs in a direction consistent with tissue recovery. Detoxification and xenobiotic metabolism pathways were restored, peroxisome-associated antioxidant systems were reactivated, and lipid metabolic pathways such as arachidonic and linoleic acid metabolism were modulated. Simultaneously, pro-inflammatory signaling axes such as cytokine–cytokine receptor interaction, IL-17, TNF, and MAPK signaling pathways were attenuated. Collectively, these findings indicate that EcN_{Tyr} alleviated radiation-induced intestinal injury through coordinated attenuation of inflammatory amplification and re-establishment of metabolic and redox balance, thereby promoting restoration of intestinal homeostasis (Figs. 6(f) and 6(g)).

Gene set enrichment analysis further revealed coordinated transcriptional reprogramming of redox and inflammatory response networks following EcN_{Tyr} administration. These findings indicate that EcN_{Tyr} alleviated radiation-induced oxidative and inflammatory stress (Fig. S19 in the ESM).

2.7 Innovation and translation of engineered probiotics

The innovations presented in this study can be delineated into four key aspects: (1) Technological principle innovation: the development of a self-reinforcing "engineered probiotic-melanin" targeting system has leveraged the synergistic effects of F1 pilus-specific colonization and melanin-mucin anchoring to achieve a dual enhancement of *in situ* synthesis and targeted retention; (2) delivery system innovation: the optimization of metabolic pathways through key gene knockout and enzyme engineering, resulted in an enhancement of melanin biosynthesis efficiency by over threefold, thereby addressed the dose-dependent limitations associated with traditional exogenous delivery methods; (3) nano enzyme cascade protection: Melanin nanoparticles serve as "molecular sponges" to neutralize free radicals, so safeguarding the activity of engineered probiotics; and (4) functional integration innovation: the pioneering combination of nanoMel antioxidant activity, microbial metabolism regulation, and physical barrier repair into a two-way microbiota-host regulatory network. This comprehensive strategy offers a clinically translatable approach for precision therapy in ARE and further advances the innovative application of synthetic biology in the realm of radiation medical protection.

3 Conclusions

This study presents EcN_{Tyr}, a genetically engineered probiotic developed using a "synthetic biology-nanomedicine" approach for treatment of ARE. The results showed that the melanin nanoMel, produced by EcN_{Tyr} has excellent biocompatibility, broad-spectrum free radical scavenging capacity, and robust stability in gastrointestinal simulants. EcN_{Tyr} showed satisfactory colonization at the inflamed site and prolonged local retention, and it significantly alleviated radiation-induced intestinal injury. The therapeutic effect of EcN_{Tyr} was attributed to the combined effect of multiple mechanisms including downregulating peroxisome-related pro-inflammatory pathways, mitigating oxidative stress and inflammation, restoring gut microbiota balance, and regulating genes associated with intestinal barrier repair. Our results indicate that oral administration of melanin-based biomimetic agents is a feasible, safe, and efficacious strategy for radiation-induced intestinal injury.

4 Prospects

Given that oral administration of EcN_{Tyr} exhibits satisfactory therapeutic efficacy in ARE treatment, a comprehensive investigation into the correlation between therapeutic efficacy and treatment regimen, such as administration timing, modality, dosage, and frequency, is essential. This initiative seeks to optimize ARE relief through more suitable administration strategies, reduced dosages, and lower frequency of administration. These measures aim to minimize potential side effects, enhance safety, and provide empirical support to accelerate the clinical translation process.

5 Experimental

5.1 Construction and culture of genetically engineered probiotics EcN_{Tyr}

5.1.1 Gene knockout

sgRNA target sites and homologous arm primers for the *pheA*, *trpR*, and *pykA* genes were synthesized, using a pUC19 EcoRI-HindIII linearized vector as the backbone. Genomic DNA from *E. coli* Nissle 1917 served as the template, and homologous arms were amplified in a 25 μL reaction containing 2× pfu PCR mix, 2 μL each primer, and 2 μL template DNA. The amplified homologous arms

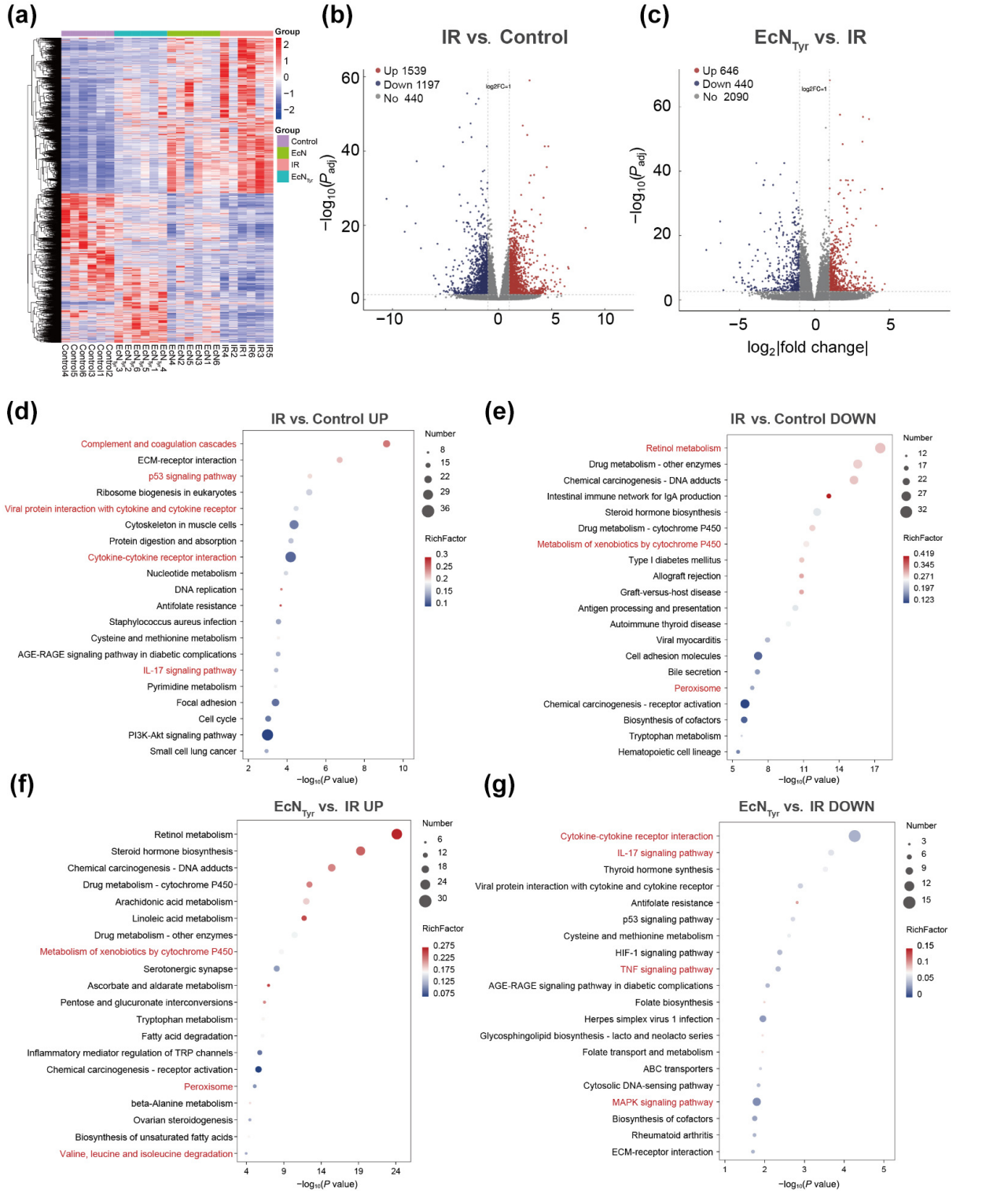

Figure 6 Transcriptome sequencing analysis of the EcN_{Tyr} treatment in the ARE mouse model. (a) Heatmap of differentially expressed genes in the EcN_{Tyr} treatment, EcN treatment, IR, and healthy control groups (P_{adj} < 0.05 and |fold change| ≥ 1). (b) Volcano plot of differentially expressed genes in the IR group compared to the control. (c) Volcano plot of differentially expressed genes in the EcN_{Tyr} treatment group compared to the IR group (P_{adj} < 0.05 and |fold change| ≥ 1). Bubble plots of KEGG (d) up- and (e) down-regulated pathways of differentially expressed genes in the IR group versus the control group. Bubble plots of KEGG (f) up- and (g) down-regulated pathways of differentially expressed genes in the EcN_{Tyr} treatment group compared with the IR group. n = 6 each group.

were ligated into the digested vector using 2 μL of 5× infusion mix, with 2 μL vector and 3 μL each homologous arm, followed by incubation on ice for 30 min before transformation into *E. coli* DH5α. Transformants were plated on Amp-IPTG-X-gal plates for screening and confirmed by sequencing. Electrocompetent *E. coli* Nissle 1917 cells were prepared, and a Cas9-expressing plasmid was introduced via electroporation (2500 V) onto kanamycin-containing plates. Subsequently, sgRNA plasmids and homology-

directed repair templates were co-transformed onto kanamycin/spectinomycin plates. Δ*pheA*, Δ*pheA*, Δ*trpR*, and Δ*pheA*Δ*trpR*Δ*pykA* were confirmed by PCR and sequencing. The plasmid-based editing tools were eliminated through serial passaging to obtain homozygous knockout bacteria. The PCR primer sequences used in this study are shown in Table S1 in the ESM.

5.1.2 Insertion and construction of VsTYR

The *VsTYR* gene (M235A/N229H mutant) (Text S1 in the ESM) from *Verrucomicrobium spinosum* was codon-optimized for *E. coli*, to construct the pUKTAC expression plasmid, including the tac promoter (Fig. S1 in the ESM). The recombinant plasmid was introduced into *E. coli* Nissle 1917 and the Δ*pheA*Δ*trpR*Δ*pykA* (Text S2 in the ESM) knockout bacteria by electroporation at 2500 V, followed by plating on kanamycin-containing agar plates. Colony PCR identification was performed using pUKTAC-JD-F/R primers in a 10 μL reaction containing 2× Taq PCR mix, 0.5 μL each primer, and 0.5 μL bacterial culture. Positive clones were identified and selected for further analysis.

5.1.3 Culture and storage of positive clones

Positive clones were inoculated into Luria-Bertani (LB) medium supplemented with kanamycin and incubated at 37 °C with shaking at 150 rpm. Single colonies were isolated by streak plating. Cultures were grown to an OD_{600} of 0.6–0.8, harvested by centrifugation at 4000 rpm for 10 min, and the cell pellets were resuspended in 1 mL of cryopreservation solution. The suspensions were stored at −80 °C for long-term preservation.

5.2 Synthesis of melanin production

The positive clones were inoculated into 5 mL LB plus kanamycin (50 μg/mL) liquid medium and cultured overnight. The next day, 1% (v/v) was transferred to 100 mL of LB liquid medium, with 5 mg $CuSO_4{\cdot}5H_2O$, 120 mg tyrosine, 5 mg kanamycin. The culture was incubated overnight at 37 °C with continuous shaking (150 rpm), during which the medium developed a distinct dark brownish-black coloration, confirming melanin biosynthesis. For melanin nanoparticle (nanoMel) isolation, the bacterial culture was sequentially processed through 0.22 μm membrane filtration and centrifuged at 11,000 rpm for 10 min. The supernatant was acidified with 6 M hydrochloric acid (1:3 v/v) and allowed to precipitate at room temperature for 10 h. Purified nanoMel was acquired via centrifugation-resuspension in deionized water for five cycles at 11,000 rpm for 10 min. The purified nanoMel was lyophilized to produce a black powder, with the ultimate yield determined by gravimetric analysis. Lastly, the lyophilized nanoMel was dissolved in concentrated ammonium hydroxide and concentrated by rotary evaporation to obtain the final nanoMel solution.

5.3 Detection of gastrointestinal stability and intestinal colonization

5.3.1 Free radical scavenging capacity of genetically engineered probiotics

To evaluate the EcN_{Tyr} stability in simulated digestive fluid (SDF), the gastric fluid simulant was made by dissolving sodium chloride and pepsin in deionized water to a final concentration of 32 μg/mL, then the pH was adjusted to 1.2 with hydrochloric acid. The intestinal fluid simulant was created by dissolving dipotassium hydrogen phosphate in deionized water, adding trypsin to a final concentration of 100 μg/mL, and adjusting the pH to approximately 7.5 with sodium hydroxide. The EcN_{Tyr} original bacterial culture (OD_{600} ~ 2.5) was concentrated 100-fold by centrifugation. A 200 μL aliquot of the concentrated bacterial solution was mixed with gastric fluid simulant (1:1 v/v) and incubated for 4 h to replicate stomach conditions. Following centrifugation, the resulting EcN_{Tyr} precipitate was resuspended in intestinal fluid simulant (1:1 v/v) and incubated for an additional 20 h to simulate the period of intestinal transit post-oral delivery. The final product was designated as SDF-treated EcN_{Tyr} (SDF-EcN_{Tyr}).

ESR spectroscopy was employed to evaluate the free radical scavenging capacities of EcN_{Tyr} and SDF-EcN_{Tyr} against DPPH·, ·OH, O_2^-, H_2O_2, and ·NO. A 10 mM ethanolic DPPH solution was produced for the experiments, and 100 mM 5,5-dimethyl-1-pyrroline *N*-oxide (DMPO) served as the spin trap. Superoxide radicals (O_2^-) were generated by the reaction of 10 mM xanthine with xanthine oxidase (1 U/mL), using 100 mM DMPO as the spin trapping agent. Hydroxyl radicals (·OH) were produced through the Fenton reaction between ferrous ions and H_2O_2, with DMPO serving as the spin trap. The H_2O_2 source was prepared by combining 400 μL of 20 mM H_2O_2 with 100 μL deionized water, with subsequent deoxygenation for 30 min to remove dissolved oxygen. Nitric oxide (·NO) was generated from 10 mM S-nitroso-N-acetyl-DL-penicillamine, with 100 mM 2-(4-carboxyphenyl)-4,4,5,5-tetramethylimidazoline-1-oxyl-3-oxide potassium salt (CITO) serving as the spin trap for both H_2O_2 and ·NO detection. Following incubation with 200 μg/mL EcN_{Tyr} and SDF-EcN_{Tyr} for 10 min, samples were transferred to ESR quartz tubes, degassed through freeze-pump-thaw cycles, and analyzed at room temperature.

5.3.2 Colony formation assay

EcN_{Tyr} cultures were grown at 37 °C with shaking at 200 rpm to the logarithmic phase (OD_{600} ~ 0.6), harvested by centrifugation, and resuspended in PBS to a final concentration of 1×10^{10} CFU/mL. To simulate gastrointestinal transit, the bacterial suspension was mixed with simulated gastric fluid at a 1:1 (v/v) ratio and incubated at 37 °C with shaking at 150 rpm for 20 min. The bacteria were then collected by centrifugation and resuspended in simulated intestinal fluid, followed by further incubation at 37 °C with shaking at 150 rpm for 2 h.

Treated probiotic suspension was diluted with PBS to an appropriate concentration, plated onto selective LB plates in triplicate, and incubated at 37 °C for 12–16 h before colony counting. Probiotic viability after simulated gastrointestinal treatment was assessed by a colony-forming units (CFU) assay.

5.3.3 In vivo and ex vivo fluorescence imaging for intestinal colonization analysis

To evaluate the intestinal colonization and retention behavior of engineered probiotics *in vivo,* EcN and EcN_{Tyr} were fluorescently labeled with IR-dye800. Specifically, bacteria in the logarithmic growth phase were collected, washed with PBS, and incubated with IR-dye800 dye under gentle shaking in the dark. Excess dye was removed by repeated centrifugation and washing.

A radiation-induced enteritis mouse model was established using the method described above. Mice were orally administered IR-dye800-labeled EcN or EcN_{Tyr} by gavage. At predetermined time points (0, 2, 4, 8, and 24 h after administration), whole-body fluorescence imaging was performed using IVIS. For *ex vivo*

analysis, intestinal tissues were excised, rinsed with PBS to remove luminal contents, and subjected to fluorescence imaging and Fontana-Masson staining. For histological fluorescence analysis, intestinal tissues were fixed with 4% paraformaldehyde, embedded, sectioned, and observed under a fluorescence microscope.

5.4 Evaluation of anti-oxidative stress capacity of genetically engineered probiotics

5.4.1 Detection of nanoMel's capacity to scavenge intracellular ROS

The procedures of cell culture were depicted in Text S3 in the ESM. RAW264.7 cells and Hiec cells were inoculated in confocal dishes. Following a 12 h incubation, 100 ng/mL lipopolysaccharide was administered to stimulate RAW264.7 cells for 24 h, while 250 μM H_2O_2 was introduced to stimulate Hiec cells for 2 h, thereby inducing reactive oxygen species generation and oxidative stress. The cells were rinsed three times with PBS, and the addition of nanoMel to continue incubation for 12 h and washed with PBS three times again. Cells without any treatment were used as control. The cells were washed three times with PBS and stained with 4',6-diamidino-2-phenylindole (DAPI) for 10 min, then washed three times again. A 10 μM fluorescent probe DCFH-DA, was introduced and incubated for 30 min at 37 °C under light protection, after which the cells were washed three times with PBS. Fluorescence confocal microscopy was performed to observe the fluorescence intensity of DCFH-DA in the cells (Ex/Em = 488/525 nm).

5.4.2 Tissue immunofluorescence ROS staining gross process

Three days after treatment, mice in all groups were euthanized by CO_2 asphyxiation. Small intestinal tissues were collected and immediately frozen in liquid nitrogen. For ROS staining, intestinal tissues were dehydrated and cleared, then incubated in ROS staining working solution. After washing to remove the unbound stain, tissues were stained with DAPI for 8 min. Following dehydration, samples were mounted on slides and observed under an inverted microscope for imaging.

5.4.3 Determination of oxidative stress-related indices in small intestinal tissues

Three days post-treatment, small intestinal tissues were immediately excised, weighed, and homogenized in 4 °C phosphate-buffered saline (PBS). The homogenates were centrifuged at 3000 rpm for 20 min at 4 °C to obtain supernatant fractions. Oxidative stress biomarkers including myeloperoxidase (MPO), superoxide dismutase (SOD), catalase (CAT), glutathione peroxidase (GPX), and malondialdehyde (MDA) were quantitatively analyzed in the intestinal tissue supernatants using standardized assays.

5.5 Safety evaluation of biomimetic engineered probiotics

Human intestinal epithelial Hiec and RAW264.7 mouse monocyte macrophage leukemia cells were purchased from the cell bank of the Chinese Academy of Science (Shanghai, China). Male Balb/c mice (6–8 weeks old, 18–22 g) and male C57BL/6J mice (6–8 weeks old, 18–22 g) were provided by Charles River Laboratories (Beijing, China).

Cell viability assay, hematological analysis, and histological evaluation were performed following standard protocols to assess the *in vitro* and *in vivo* safety of nanoMel and EcN_{Tyr}. Detailed experimental procedures are provided in Text S4 in the ESM.

5.6 Analysis of therapeutic efficacy of genetically engineered probiotics

5.6.1 Establishment of the ARE mouse model

The 6–8 weeks old male Balb/c mice were abdominally irradiated to X-rays at a dose rate of 10 mGy/s (220 mV, 13 mA) to a total dose of 10 Gy for establishing the ARE model. Mice were randomly divided into 3 groups: (1) Healthy control (no treatment); (2) ARE model (X-ray irradiation only); (3) EcN_{Tyr} treatment (X-ray irradiation + EcN_{Tyr}). EcN_{Tyr} administered via oral gavage 24 and 6 h before X-ray irradiation. The dosage was based on OD_{600} (protoplasmic fluid at 2–2.5, concentrated 100-fold), given at 10 μL/g mouse body weight, 3 days after the different treatment protocols.

5.6.2 Immunohistochemical and H&E analysis

Three days after treatment completion, small intestinal tissues were collected and fixed in 4% paraformaldehyde. Sections were prepared at 5 μm thickness and then deparaffinized. The intestinal tissue sections were subjected to immunohistochemical staining following standard procedures. The general procedure for immunohistochemical staining is described in Text S5 in the ESM. Tissue sections were immersed in hematoxylin staining solution for 3 min, stained with eosin for 1 min, dehydrated, sealed, observed by inverted microscope, photographed and scored (see Table S2 in the ESM for detailed scoring criteria).

5.7 Effects of genetically engineered probiotics on inflammatory factors

Three days post-treatment, small intestinal tissues were collected, weighed and homogenized in PBS on ice. The homogenate was subsequently centrifuged at 3000 rpm for 20 min at 4 °C, and the supernatant was retrieved. The expression levels of representative inflammatory factors, comprising IL-6, IL-8, TNF-α, IL-1β and IL-10, were detected in the small intestinal tissue homogenate.

5.8 Effect of genetically engineered probiotics on intestinal barrier integrity

Small intestinal tissues were obtained from each group of mice and fixed in 4% paraformaldehyde. The samples underwent citric acid antigen retrieval, endogenous peroxidase inactivation, and antigen blocking. Primary antibodies were incubated overnight at 4 °C, then secondary antibodies were applied at 37 °C for 30 min, and nuclei were stained with DAPI for 8 min. After dehydration and mounting, samples were observed under a fluorescence microscope. Fluorescence signal intensity was analyzed from captured images. The antibodies dilution ratios were ZO-1 (1:200, GB111402, Servicebio), occludin (1:200, DF7504, Affinity), and claudin-1 (1:200, ab242370, Abcam).

5.9 Fecal gut microbiota analysis

The procedures for fecal sample collection, DNA extraction, and bioinformatics analysis are shown in Text S6 in the ESM.

5.9.1 16S rDNA amplification and sequencing

341F (5'-CTACGGGNGGCWGCAG-3') and 805R (5'-ACTACHVGGGTATCTAATCC-3') were used as primers to amplify the V4 region, and PCR amplification, product recovery and fluorescence quantification were performed according to the

standard process; the library was constructed using the TruSeq DNA PCR-Free Kit, and after quality control by Agilent 2100, it was diluted to 12 pM for HiSeq sequencing.

The V4 region of bacterial 16S rRNA was amplified using universal primers 341F (5'-CCTACGGGNGGCWGCAG-3') and 805R (5'-GACTACHVGGGTATCTAATCC-3'), followed by PCR standard amplification process, including product purification, and fluorescence quantification. Subsequently, libraries for sequencing were constructed with the TruSeq DNA PCR-Free Kit. Following quality assessment with the Agilent 2100, qualified libraries were diluted to 12 pM for HiSeq sequencing.

5.10 Transcriptome experimental analysis

Three days after treatment, the mice were euthanized with carbon dioxide, and the small intestinal tissues of the mice in the four groups (control, IR, IR+EcN, IR+EcN$_{Tyr}$, $n = 6$ for each group) were obtained for nucleic acid extraction and whole transcriptome sequencing.

5.11 Statistical analysis

All experiments were repeated at least three times. Measurements were expressed as mean ± standard deviation. Statistical analysis was performed using Student's unpaired t-test with GraphPad Prism 8.2.1 software. ns: not significant, $^{*}P < 0.05$, $^{**}P < 0.01$, $^{***}P < 0.001$. For microbiota and transcriptome analyses involving multiple features, *P*-values were adjusted for multiple comparisons using the Benjamini–Hochberg false discovery rate (FDR) correction.

Electronic Supplementary Material: Supplementary material (further details of engineered probiotics construction and nanoMel characterization, gastrointestinal stability and colonization assays, biosafety evaluation, gut microbiota analysis, and transcriptome sequencing analysis) is available in the online version of this article at https://doi.org/10.26599/NR.2026.94908605.

Data availability

All data needed to support the conclusions in the paper are presented in the manuscript and the Electronic Supplementary Material. Additional data related to this paper may be requested from the corresponding author upon request.

Acknowledgements

This research received funding from the Xuanwu Hospital Talent Convergence Program (No. HZ2025PYYX006), Capital Medical University Research and Development Fund (No. PYZ25038), and the National Natural Science Foundation of China (No. 82001889). The animal study protocol was approved by the Institutional Animal Care and Use Committee at Capital Medical University. We thank biorender.com for helping create the table of contents.

Declaration of competing interest

Y. L. and J. L. have a pending patent application (No. 2025106547725). All other authors declare that they have no known competing financial interests or personal relationships that could have appeared to influence the work reported in this paper.

Author contribution statement

Y. L.: Writing – original draft, methodology, investigation, formal analysis, funding acquisition, conceptualization. M. H.: Writing – original draft, formal analysis, methodology. J. H.: Project administration, resources, visualization. Z. Y.: Data curation, preliminary analysis. Y. T. Z.: Data curation, preliminary analysis. R. Y. C.: Supervision, methodology. F. Y.: Validation, investigation. J. L.: Writing – review & editing, supervision, project administration, funding acquisition.

Informed consent

Not applicable.

Ethics statement

Not applicable.

Use of AI statement

None.

References

[1] Leonetti, D.; Estéphan, H.; Ripoche, N.; Dubois, N.; Aguesse, A.; Gouard, S.; Brossard, L.; Chiavassa, S.; Corre, I.; Pecqueur, C. et al. Secretion of acid sphingomyelinase and ceramide by endothelial cells contributes to radiation-induced intestinal toxicity. *Cancer Res.* **2020**, *80*, 2651–2662.

[2] Gandle, C.; Dhingra, S.; Agarwal, S. Radiation-induced enteritis. *Clin. Gastroenterol. Hepatol.* **2020**, *18*, A39–A40.

[3] Xiao, H. W.; Cui, M.; Li, Y.; Dong, J. L.; Zhang, S. Q.; Zhu, C. C.; Jiang, M.; Zhu, T.; Wang, B.; Wang, H. C. et al. Gut microbiota-derived indole 3-propionic acid protects against radiation toxicity via retaining acyl-CoA-binding protein. *Microbiome* **2020**, *8*, 69.

[4] Manichanh, C.; Varela, E.; Martinez, C.; Antolin, M.; Llopis, M.; Doré, J.; Giralt, J.; Guarner, F.; Malagelada, J. R. The gut microbiota predispose to the pathophysiology of acute postradiotherapy diarrhea. *Am. J. Gastroenterol.* **2008**, *103*, 1754–1761.

[5] Yi, Y. X.; Shen, L. J.; Shi, W.; Xia, F.; Zhang, H.; Wang, Y. Q.; Zhang, J.; Wang, Y.; Sun, X. Y.; Zhang, Z. Y. et al. Gut microbiome components predict response to neoadjuvant chemoradiotherapy in patients with locally advanced rectal cancer: A prospective, longitudinal study. *Clin. Cancer Res.* **2021**, *27*, 1329–1340.

[6] Li, Y.; Dong, J. L.; Xiao, H. W.; Zhang, S. Q.; Wang, B.; Cui, M.; Fan, S. J. Gut commensal derived-valeric acid protects against radiation injuries. *Gut Microbes* **2020**, *11*, 789–806.

[7] Moraitis, I.; Guiu, J.; Rubert, J. Gut microbiota controlling radiation-induced enteritis and intestinal regeneration. *Trends Endocrinol. Metab.* **2023**, *34*, 489–501.

[8] P B, A.; Sudha, S. P.; Mohan, P.; Patil, N.; Rahman, A.; Gundapuneedi, B. S.; M, H. Racecadotril versus loperamide in acute radiation enteritis: A randomized, double-masked, phase 3, noninferiority trial. *Int. J. Radiat. Oncol. Biol. Phys.* **2024**, *118*, 616–625.

[9] Cui, M.; Xiao, H. W.; Li, Y.; Zhou, L. X.; Zhao, S. Y.; Luo, D.; Zheng, Q. S.; Dong, J. L.; Zhao, Y.; Zhang, X. et al. Faecal microbiota transplantation protects against radiation-induced toxicity. *EMBO Mol. Med.* **2017**, *9*, 448–461.

[10] Xu, M. Q.; Pan, F.; Peng, L. H.; Yang, Y. S. Advances in the isolation, cultivation, and identification of gut microbes. *Mil. Med. Res.* **2024**, *11*, 34.

[11] Cui, M.; Xiao, H. W.; Li, Y.; Zhang, S. Q.; Dong, J. L.; Wang, B.; Zhu, C. C.; Jiang, M.; Zhu, T.; He, J. B. et al. Sexual dimorphism of gut microbiota dictates therapeutics efficacy of radiation injuries. *Adv.*

Sci. **2019**, *6*, 1901048.
[12] Zhu, P. P.; Lu, T. K.; Wu, J. Y.; Fan, D. D.; Liu, B. Y.; Zhu, X. X.; Guo, H.; Du, Y.; Liu, F.; Tian, Y. et al. Gut microbiota drives macrophage-dependent self-renewal of intestinal stem cells via niche enteric serotonergic neurons. *Cell Res.* **2022**, *32*, 555–569.
[13] Jain, U.; Lai, C. W.; Xiong, S. S.; Goodwin, V. M.; Lu, Q. H.; Muegge, B. D.; Christophi, G. P.; VanDussen, K. L.; Cummings, B. P.; Young, E. et al. Temporal regulation of the bacterial metabolite deoxycholate during colonic repair is critical for crypt regeneration. *Cell Host Microbe* **2018**, *24*, 353–363.e5.
[14] Schirmer, M.; Garner, A.; Vlamakis, H.; Xavier, R. J. Microbial genes and pathways in inflammatory bowel disease. *Nat. Rev. Microbiol.* **2019**, *17*, 497–511.
[15] Rubert, J.; Schweiger, P. J.; Mattivi, F.; Tuohy, K.; Jensen, K. B.; Lunardi, A. Intestinal organoids: A tool for modelling diet-microbiome-host interactions. *Trends Endocrinol. Metab.* **2020**, *31*, 848–858.
[16] Guo, P. L.; Wang, W. J.; Xiang, Q.; Pan, C.; Qiu, Y. F.; Li, T. T.; Wang, D. F.; Ouyang, J.; Jia, R. R.; Shi, M. et al. Engineered probiotic ameliorates ulcerative colitis by restoring gut microbiota and redox homeostasis. *Cell Host Microbe* **2024**, *32*, 1502–1518.e9.
[17] Lin, S. S.; Mukherjee, S.; Li, J. J.; Hou, W. L.; Pan, C.; Liu, J. Y. Mucosal immunity-mediated modulation of the gut microbiome by oral delivery of probiotics into Peyer's patches. *Sci. Adv.* **2021**, *7*, abf0677.
[18] Merenstein, D.; Pot, B.; Leyer, G.; Ouwehand, A. C.; Preidis, G. A.; Elkins, C. A.; Hill, C.; Lewis, Z. T.; Shane, A. L.; Zmora, N. et al. Emerging issues in probiotic safety: 2023 perspectives. *Gut Microbes* **2023**, *15*, 2185034.
[19] Foley, M. H.; O'Flaherty, S.; Allen, G.; Rivera, A. J.; Stewart, A. K.; Barrangou, R.; Theriot, C. M. *Lactobacillus* bile salt hydrolase substrate specificity governs bacterial fitness and host colonization. *Proc. Natl. Acad. Sci. USA* **2021**, *118*, e2017709118.
[20] Beyaz, S.; Mana, M. D.; Roper, J.; Kedrin, D.; Saadatpour, A.; Hong, S. J.; Bauer-Rowe, K. E.; Xifaras, M. E.; Akkad, A.; Arias, E. et al. High-fat diet enhances stemness and tumorigenicity of intestinal progenitors. *Nature* **2016**, *531*, 53–58.
[21] Shen, H. S.; Aggarwal, N.; Wun, K. S.; Lee, Y. S.; Hwang, I. Y.; Chang, M. W. Engineered microbial systems for advanced drug delivery. *Adv. Drug Del. Rev.* **2022**, *187*, 114364.
[22] Li, Z. T.; Wang, Y. X.; Liu, J.; Rawding, P.; Bu, J.; Hong, S.; Hu, Q. Y. Chemically and biologically engineered bacteria-based delivery systems for emerging diagnosis and advanced therapy. *Adv. Mater.* **2021**, *33*, e2102580.
[23] Zhou, J.; Li, M. Y.; Chen, Q. F.; Li, X. J.; Chen, L. F.; Dong, Z. L.; Zhu, W. J.; Yang, Y.; Liu, Z.; Chen, Q. Programmable probiotics modulate inflammation and gut microbiota for inflammatory bowel disease treatment after effective oral delivery. *Nat. Commun.* **2022**, *13*, 3432.
[24] Asgari, S.; Pourjavadi, A.; Licht, T. R.; Boisen, A.; Ajallouean, F. Polymeric carriers for enhanced delivery of probiotics. *Adv. Drug Del. Rev.* **2020**, **161–162**, 1–21.
[25] Yang, X. Y.; Yang, J. L.; Ye, Z. H.; Zhang, G. Z.; Nie, W. M.; Cheng, H.; Peng, M. Y.; Zhang, K. X.; Liu, J. J.; Zhang, Z. Z. et al. Physiologically inspired mucin coated escherichia coli nissle 1917 enhances biotherapy by regulating the pathological microenvironment to improve intestinal colonization. *ACS Nano* **2022**, *16*, 4041–4058.
[26] Larabi, A. B.; Masson, H. L. P.; Bäumler, A. J. Bile acids as modulators of gut microbiota composition and function. *Gut Microbes* **2023**, *15*, 2172671.
[27] Wang, M. W.; Yang, J.; Li, M.; Wang, Y. F.; Wu, H.; Xiong, L.; Sun, Q. J. Enhanced viability of layer-by-layer encapsulated Lactobacillus pentosus using chitosan and sodium phytate. *Food Chem.* **2019**, *285*, 260–265.
[28] Liu, Y.; Gao, P. L.; Jia, X. H.; Jiang, J. Y.; Hui, H.; Tian, J. Oral-administered allomelanin-like nanomedicine with multi-enzyme mimesis and favorable gastrointestinal tolerance for amelioration of acute colitis. *Appl. Mater. Today* **2024**, *37*, 102143.
[29] Liu, H.; Yang, Y. Y.; Liu, Y.; Pan, J. J.; Wang, J. Q.; Man, F. Y.; Zhang, W. G.; Liu, G. Melanin-like nanomaterials for advanced biomedical applications: A versatile platform with extraordinary promise. *Adv. Sci.* **2020**, *7*, 1903129.
[30] Beach, M. A.; Nayanathara, U.; Gao, Y. T.; Zhang, C. H.; Xiong, Y. J.; Wang, Y. F.; Such, G. K. Polymeric nanoparticles for drug delivery. *Chem. Rev.* **2024**, *124*, 5505–5616.
[31] Xiao, Y.; Wang, D. D.; Luo, B.; Chen, X.; Yao, Y. Z.; Song, C.; Wu, M. C.; Li, P. Z.; Li, X. Y.; Zhang, H. et al. *In-situ* synthesis of melanin in tumor with engineered probiotics for hyperbaric oxygen-synergized photothermal immunotherapy. *Nano Today* **2022**, *47*, 101632.
[32] Song, W. J.; He, Y. L.; Feng, Y. N.; Wang, Y. Y.; Li, X. Y.; Wu, Y. N.; Zhang, S. X.; Zhong, L.; Yan, F.; Sun, L. T. Image-guided photothermal and immune therapy of tumors via melanin-producing genetically engineered bacteria. *Small* **2024**, *20*, e2305764.
[33] Liu, Y.; Huang, X. Z.; Jia, X. H.; Huang, J.; Cao, R. Y.; Yu, F.; Xue, K. Z.; Hui, H.; Lu, J. Biosynthesis of melanin with engineered probiotics for oral treatment of ulcerative colitis. *ACS Nano* **2025**, *19*, 21333–21347.
[34] Xie, W. J.; Dhinojwala, A.; Gianneschi, N. C.; Shawkey, M. D. Interactions of melanin with electromagnetic radiation: From fundamentals to applications. *Chem. Rev.* **2024**, *124*, 7165–7213.
[35] Zou, Y.; Chen, X. F.; Yang, P.; Liang, G. J.; Yang, Y.; Gu, Z. P.; Li, Y. W. Regulating the absorption spectrum of polydopamine. *Sci. Adv.* **2020**, *6*, eabb4696.
[36] Chen, Y.; Che, J. Y.; Wang, J. G.; Tuo, Y.; Zhao, H. Y.; Chen, Y.; Sai, L.; Zhao, H. F.; Zhang, R. P. Functional melanin nanoparticles-assisted laser desorption ionization mass spectrometry for high-sensitivity detection of TBBPA and TBBPS contaminations in animal-derived foodstuffs. *J. Agric. Food Chem.* **2024**, *72*, 6744–6753.
[37] Zhao, J.; Tang, Z.; Jiang, Y. C.; Yang, Y. J.; Liao, J. B.; Su, Z. J.; Usman, A. M.; Chen, X. Y.; Xiao, G. L. Oxidative stress in hydrocephalus: A new potential therapeutic target. *Brain-X* **2024**, *2*, e70008.
[38] Ouyang, K. S.; Puschhof, J. Sticky situation: How adhesive bacteria drive colon cancer. *Nature* **2024**, *635*, 298–299.
[39] Zuo, Y. M.; Ying, Y. B.; Huang, Z. Y.; Shen, J. M.; Li, X. K.; Wang, Z. G. Reactive oxygen species targeted biomaterials for spinal cord injury therapy. *Brain-X* **2023**, *1*, e32.